Optical Materials 35 (2013) 2721–2727

Contents lists available at ScienceDirect

Optical Materials

journal homepage: www.elsevier.com/locate/optmat

Optical and structural properties of nanostructured ZnO thin films deposited onto FTO/glass substrate by a solution-based technique

M. Berruet [a,*], C.J. Pereyra [b], G.H. Mhlongo [c], M.S. Dhlamini [c,d], K.T. Hillie [c,e], M. Vázquez [a], R.E. Marotti [b]

[a] División Electroquímica y Corrosión, INTEMA, Facultad de Ingeniería, CONICET-Universidad Nacional de Mar del Plata, J.B. Justo 4302, B7608FDQ Mar del Plata, Argentina
[b] Instituto de Física and CINQUIFIMA, Facultad de Ingeniería, Universidad de la República, Herrera y Reissig 565, C.C. 30, 11000 Montevideo, Uruguay
[c] National Centre for Nano-Structured Materials, Council for Scientific and Industrial Research, 1-Meiring Naude Road, Brummeria, P.O. Box 395, Pretoria 0001, South Africa
[d] Department of Physics, University of South Africa, P.O. Box 392, UNISA 0003, South Africa
[e] Department of Physics, University of the Free State, P.O. Box 339, Bloemfontein ZA9300, South Africa

ARTICLE INFO

Article history:
Received 21 May 2013
Received in revised form 24 July 2013
Accepted 20 August 2013
Available online 12 September 2013

Keywords:
Nanostructured ZnO
Thin film
Sol–gel based growth
Optical property
Photoluminescence

ABSTRACT

Nanostructured zinc oxide thin films were spin coated on conductive glass substrates via a sol–gel based technique using zinc acetate dihydrate as precursor. The pH of the alkalis used as catalytic agents in the hydrolysis step is shown to have a strong effect on the structural and morphological properties of the deposited ZnO. The size of the particles was observed by Transmission Electron Microscopy (TEM), while Focused Ion Beam-Scanning Electron Microscopy (FIB-SEM) and Atomic Force Microscopy (AFM), were used to analyze the morphology of the films. X-ray diffraction (XRD) and Raman spectra provided evidence of crystal growth together with an increase in the crystalline degree of the hexagonal wurtzite structure after annealing. The bandgap energy was estimated by Tauc's method and found to decrease after annealing, which is attributed to an increase in the crystallite size and to the presence of less defect sites. A good correlation between crystallite size and absorption edges was found. The photoluminescence spectra of as-deposited samples depend on the nature and pH values of catalytic agent used, and reveal the presence of a broad visible emission attributed to a variety of intrinsic defects.

1. Introduction

ZnO is a versatile n-type transparent II–VI semiconductor [1,2] with excellent properties for applications in solid-state sensors, light-emitting diodes, transparent electrodes, photocatalysts and photovoltaic devices [3–7]. In many of these applications the presence of nanostructured ZnO introduces further advantages [1,7,8].

The control of the dimension and morphology of nano- and micro-structured materials with optical and electronic properties attracts permanent interest in the research community, aiming at the design of functional devices. In particular, ZnO nanoparticles merit special attention in all applications of ZnO where size control at the nanoscale is important. For example, in nanowire arrays grown onto a seed layer, the nanowire diameter is directly related to the nanoparticle size of the seed layer [1]. Another well-known example is in luminescent devices because of the bandgap tunability that results from quantum confinement effects [9].

Another interesting property of ZnO is its ability to emit light at different spectral regions that can be analyzed by photoluminescence (PL). The near band edge UV emissions have been extensively studied and are well understood [9,10]. However, the many visible luminescence (VL) emissions (blue, green, yellow, orange and red spectral range), although currently intensely studied, are still not completely understood. They are certainly associated to below-gap states that must be related to defects. Their origin and the corresponding energy levels of the electronic states are controversial [4,11,12]. Furthermore, it has been shown that VL emissions even depend on the morphology of the nanostructures [12–14].

In this context, the structural and optical properties of ZnO thin films have a strong dependence on the deposition method as well as on the experimental parameters. So far, ZnO-based thin films have been prepared by many different techniques based on vacuum deposition and solution-based processes. Solution-based deposition processes offer a simple, low cost, and large area thin-film coating alternative to vacuum deposition techniques. For instance, sol–gel based methods not only enable easy fabrication of a large area thin film at a low cost, but can also be used to control the film composition. A homogeneous composition can be guaranteed due to the mixing of liquid precursors and a uniform thickness can be achieved with relatively simple equipment. The properties of ZnO thin films prepared by sol–gel have been found to depend on the sol concentration [15], heat-treatment conditions [16], substrate [17], film thickness [18] and dopants [19]. Ilican et al. [20] and Rani et al. [21] studied the effect of pH on the

* Corresponding author. Tel.: +54 223 481 6600x244; fax: +54 223 481 0046.
E-mail address: mberruet@fi.mdp.edu.ar (M. Berruet).

0925-3467/$ - see front matter © 2013 Elsevier B.V. All rights reserved.
http://dx.doi.org/10.1016/j.optmat.2013.08.018

structural and morphological properties of undoped ZnO films and found the optimum pH value for the film formation.

In the present investigation, we report a method to deposit nanocrystalline ZnO thin films using a simple and inexpensive sol–gel based technique. This study focuses on the effect of pH and annealing on the structural, morphological and optical properties of the films. A fluorine doped tin oxide (FTO) transparent conductive layer over glass was used as substrate for the eventual application of present samples in electrochemical experiments.

2. Experimental

2.1. Sol–gel based synthesis

0.0025 mol of $Zn(CH_3COO)_2{\cdot}2H_2O$ were dissolved in 30 mL of boiling absolute ethanol and stirred, which results in a transparent solution (Solution A). In due time, evaporated ethanol was replaced, so as to keep the volume constant. Simultaneously, 0.005 mol of XOH (X: Na or Li) were dissolved in 10 mL of absolute ethanol at 40 °C in an ultrasonic bath (Solution B). Both solutions were cooled in a mixture of ice and water. Solution B was added drop by drop into Solution A under vigorous stirring. After reacting for 30 min, a clear sol was obtained with pH = 11 when X: Na and pH = 8 when X: Li. The sol was kept at room temperature to complete the gelation and hydrolysis process, leading to the formation of a light-green colored powder when the sol–gel material was excited with UV radiation [22].

Finally, the colloidal suspension was centrifuged and washed repeatedly with heptane to remove undesired byproducts.

2.2. Substrate

Nanocrystalline ZnO thin films were deposited on FTO/glass (glass coated with a transparent conducting fluorine doped tin oxide, SnO2:F, layer Pilkington TEC™, resistivity 8 Ω/sq, thickness 3 mm). Prior to use, the substrates were degreased with a detergent solution followed by rinsing in an ultrasonic bath with acetone, ethanol and water during 10 min in each case.

2.3. Thin films deposition

The powder obtained as described in Section 2.1 was redispersed in ethanol and then ZnO was deposited on the substrate with a spin coater (Chemal Technology, model KW-4A). The coating solution was dropped and spin-casted in air at 2000 rpm for 30 s. Then they were dried on a hot plate at 90 °C for 5 min. The procedure was repeated 5 times.

The effect of annealing has been analyzed and compared to as-deposited films. Annealing was carried out at 450 °C during 1 h in air.

Both, as-deposited and annealed films showed good adhesion and were stable over several months.

2.4. Characterization

The particles size and crystalline properties were analyzed by Transmission Electron Microscopy (TEM) using a JEOL-JEM 2100 HRTEM microscope.

The films were analyzed using X-ray diffraction (XRD) with a PANalytical X'Pert Pro diffractometer, Cu K-alpha radiation at 40 kV and 40 mA. The samples were scanned between 20° and 80° at 0.02°/s. The crystallographic data for each phase were analyzed with X'Pert HighScore™ software. The crystallite size was determined by the width of the XRD peak that corresponds to ZnO plane (1 0 1), using Scherrer's equation [23].

Raman spectroscopy was performed using an Invia Reflex confocal Raman microprobe. Excitation was provided with the 514 nm emission line of an Ar+ laser and measurements were performed in backscattering configuration using a 50× objective. The morphology of the layers was studied with Focused Ion Beam-Scanning Electron Microscopy (FIB-SEM) and Atomic Force Microscopy (AFM), using an AURIGA Cobra FIB-FESEM microscope and a Digital Instrument Nanoscope VI from Veeco, respectively.

The thickness of the films was measured using a KLA TENCOR D-100 profilometer.

The photoluminescence (PL) spectra were measured using a calibrated S2000 Ocean Optics spectrometer, and exciting with wavelengths of 250 nm, 295 nm and 345 nm (UV LEDs, ROITHNER LASERTECHNIK GmbH). A band-pass Hoya U-340 optical filter (from UQG Optics) was used before the sample to filter visible light emitted by the LED (except for 250 nm, where a Hoya U-330 from ORIEL was used instead). A long-pass Schott GG-395 optical filter (also from UQG Optics) was used to filter UV light from the LED. To guarantee proper filtering, the resulting spectra were analyzed in the region of almost null signal when measuring with a bare substrate, i. e. no PL from FTO/glass substrate was measured in this region. All the optical measurements were carried out at room temperature.

The transmittance of the thin films in the UV–Vis region was evaluated using a double beam UV–Vis spectrophotometer (Shimadzu UV-160).

3. Results and discussion

3.1. Reaction mechanism

ZnO synthesis by this sol–gel based method can be rationalized by means of a series of reactions taking place in sequential steps. These steps have been proposed to be [21]:

(i) Solvation of zinc acetate dehydrate precursor in ethanol.

(ii) Hydrolysis – X: Na, Li.

$$Zn(CH_3COO)_2 \cdot 2H_2O + 2XOH \rightarrow Zn(OH)_2 + 2CH_3COOX + 2H_2O$$

(iii) Hydration:

$$Zn(OH)_2 + 2H_2O \rightarrow Zn(OH)_4^{2-} + 2H^+$$

(iv) ZnO formation (dehydration)

$$Zn(OH)_4^{2-} \leftrightarrows ZnO + H_2O + 2OH^-$$

In the sol–gel technique, there is a pH window within which the nanostructure may be formed. In acidic solutions (pH < 7), ZnO particles do not grow due to increased solubility of ZnO. In alkaline solutions (pH > 9), the size of particles is reduced due to increased solubility of ZnO (see the equilibrium in step iv). Accordingly, the pH value is a key variable to control the formation rate of an amphoteric species such as ZnO. Consequently, pH will influence the particle size and the particle size distribution [21].

3.2. Structural and morphological properties

3.2.1. TEM

Fig. 1 presents TEM images of ZnO nanoparticles redispersed after washing in ethanol and drying. Fig. 1(a) and (b) show agglomeration of ZnO particles formed when pH = 11 (X: Na). The average diameter of the particles that can be seen in these images is 4 nm. Fig. 1(c) and (d) show monodisperse particles of ZnO formed when pH = 8 (X: Li) where the measured diameter is 5 nm, i.e., they are slightly bigger than the particles formed at pH = 11. These sizes are in good agreement with the effect of pH on particle size (described in Section 3.1). The insert in Fig. 1(d) is a magnification

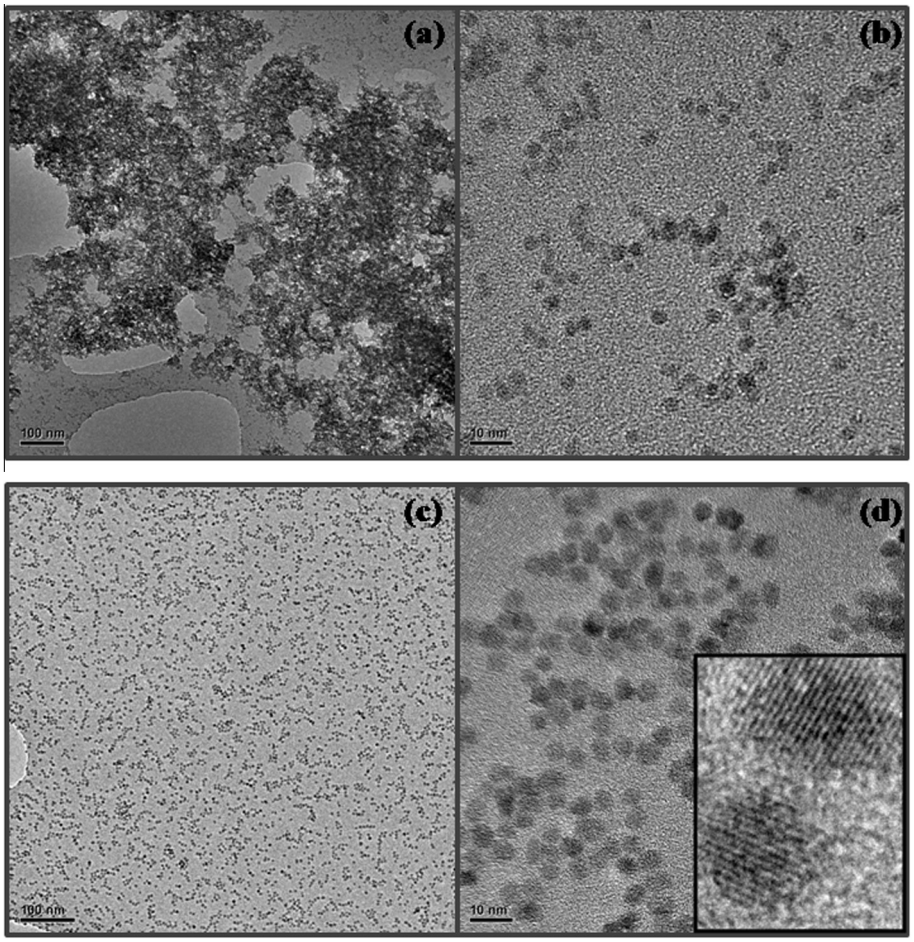

Fig. 1. TEM images of ZnO nanoparticles formed at (a), (b) pH = 11 (X: Na) and (c), (d) pH = 8 (X: Li), after drying of a dispersion in ethanol.

of the image, where defined parallel lines confirm a high degree of crystallinity. High-resolution transmission electron microscopy (HRTEM) of the fabricated ZnO nanoparticles shows a d-spacing of 0.276 nm and 0.256 nm which correspond to the (101) and (102) planes of ZnO, respectively.

3.2.2. XRD

Fig. 2 shows XRD patterns of ZnO films prepared at pH = 8 before and after annealing. ZnO thin films were prepared following the route described in Section 2.3. Both films present a hexagonal structure matching that of wurtzite (PDF 79-0207). The as-deposited film is analyzed in Fig. 2(a). The peaks are broad with low intensity, as expected for a material with low crystallinity or for a film composed by very small crystallites. This last behavior was observed previously by TEM (Fig. 1). On the other hand, annealed films (Fig. 2(b)) present sharp peaks indicating larger crystallite size of the material. The improvement after the annealing is expected and can be attributed to crystal growth. The same behavior was observed with films obtained for pH = 11 (not shown). From Fig. 2, it can be seen that the (101) is the most intense diffraction peak and is presented as one of the prominent orientations in the HRTEM images (Fig. 1(d)). This peak can therefore be used confidently to estimate the crystallite size (D) using Scherrer's equation [23]. Table 1 shows the values of the crystallite size of each of the various types of annealed and as-deposited films.

3.2.3. AFM and FIB-SEM

Fig. 3(a) and (b) show representative AFM and FIB-SEM images of ZnO films obtained at pH = 8 before and after annealing,

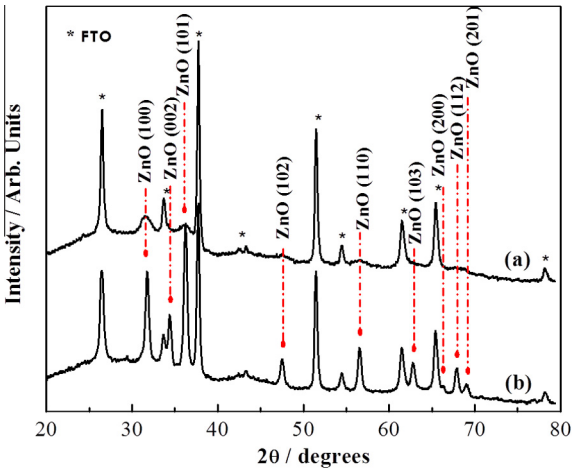

Fig. 2. XRD patterns of ZnO thin films on FTO/glass substrates prepared at pH = 8 (a) before and (b) after annealing at 450 °C. Reference patterns: wurtzite [PDF 79-0207].

respectively. The images show representative sections of different samples. Surface morphology reveals that the annealed film is formed by agglomerates of smaller size than those found in the as-deposited film. In contrast, each of these agglomerates is formed by crystallites which grow after the annealing treatment. It is clear that there is a restructuration due to the relaxation of tension forces in the nanoparticles. This results in a more stable state, where bigger crystallites are grouped into smaller agglomerates.

Table 1
Crystallite and particle size for different types of annealed and as-deposited ZnO films.

	ZnO (D (nm))			
	Hydrolysis with LiOH, pH = 8		Hydrolysis with NaOH, pH = 11	
	As-deposited	Annealed	As-deposited	Annealed
Calculated from TEM	5		4	
XRD (Scherrer)	6	18	5	23

An average roughness factor can be evaluated from the AFM results. The root mean square roughness (Rq) can be calculated from the surface features and it is found to be greater than 60 nm for the as-prepared samples. After annealing the roughness Rq drops to values below 43 nm. This could be attributed to the smoothening of the surface due to sintering.

The average thickness value of ZnO thin films after preparation at pH = 11 is 1900 nm meanwhile at pH = 8 is 500 nm. After annealing a decrease in thickness values was found but no appreciable difference was shown before and after annealing.

3.2.4. Raman

Fig. 4 presents the Raman spectra of ZnO thin films for as-deposited (pH = 8) and annealed samples (pH = 8 and 11). The pH has no significant effect for as-deposited samples. Hence, it is not shown. It can be observed that the broad peaks at 561 cm^{-1} and 630 cm^{-1} arise from the substrate [24]. Unfortunately, the peak at 561 cm^{-1} hinders the observation of the band expected at 539 cm^{-1} which should correspond to the second-order Raman spectrum arising from zone-boundary phonons 2-LA (M) [10] as well as the E_1-LO mode expected at 578 cm^{-1} that usually originates from second-order Raman scattering and the presence of impurities and/or defects. However, the E_2-high Raman mode is clearly observed at 437 cm^{-1} in every spectrum: this band can be attributed to the oxygen vibration and is one of the characteristic signals of wurtzite ZnO [10]. This E_2-high mode is better defined and more intense in the annealed samples, as expected for more crystalline ZnO thin films obtained after the thermal treatment.

3.3. Optical properties

3.3.1. Transmittance

UV–Vis transmittance spectra typical of thin films before and after annealing are presented in Fig. 5(a) and (b) for preparation at pH = 11 and 8, respectively. Fig. 5(a) shows a monotonic increase of transmittance at longer wavelength due to light scattering [2]. The same behavior is observed before and after annealing. Annealed thin films present an appreciable reduction in transmittance spectra for the whole wavelength range [25]. If this effect is originated in light scattering in the nanostructured film, larger particle diameter after annealing would increase light dispersion, diminishing transmittance accordingly. Fig. 5(b) shows that ZnO thin films prepared at pH = 8 are more transparent than those prepared at pH = 11 (Fig. 5(a)). However in this case, annealing does not decrease transmittance, as it was observed for pH = 11.

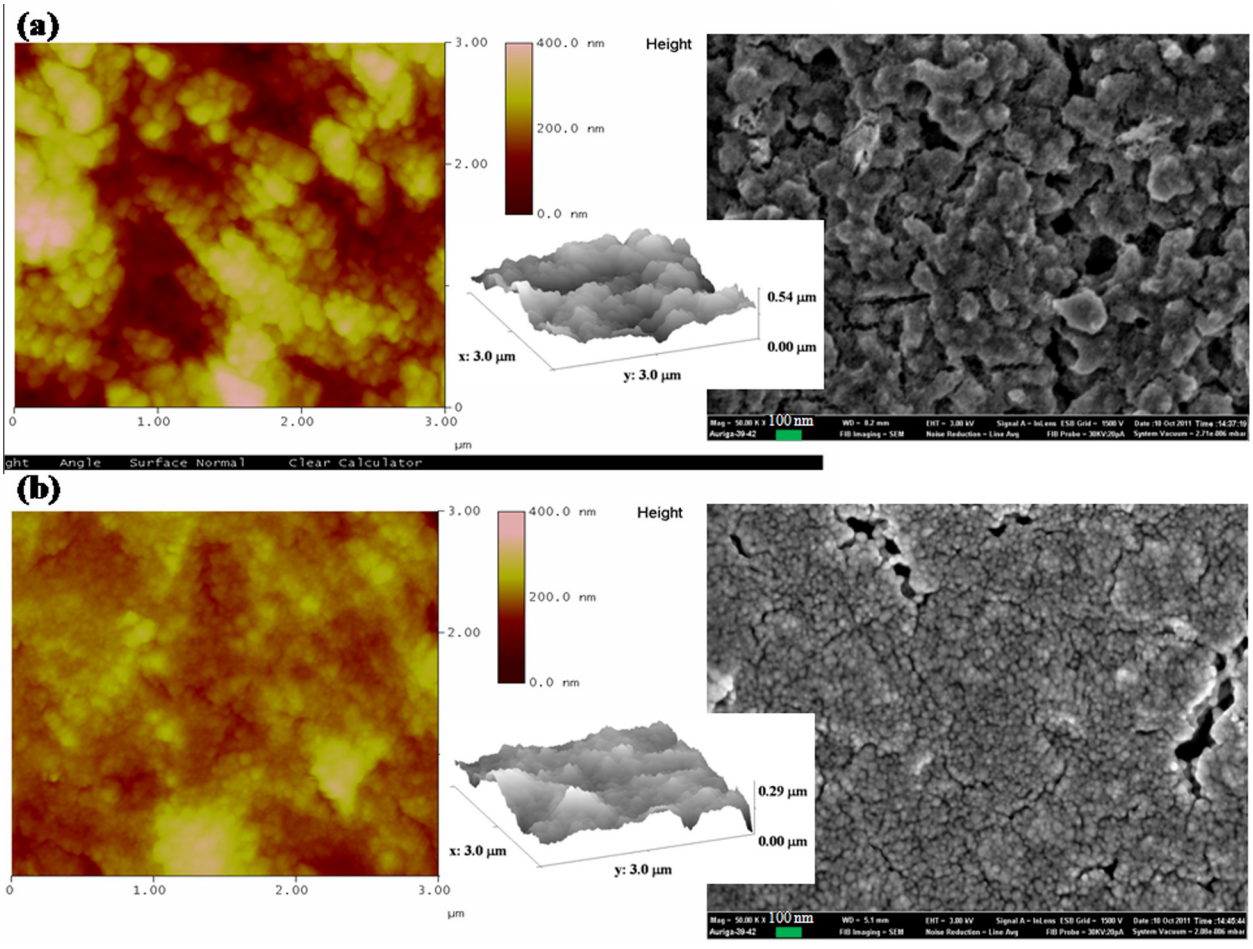

Fig. 3. AFM (left side) and FIB-SEM (right side) images of ZnO thin films prepared at pH = 8 (a) before and (b) after annealing at 450 °C.

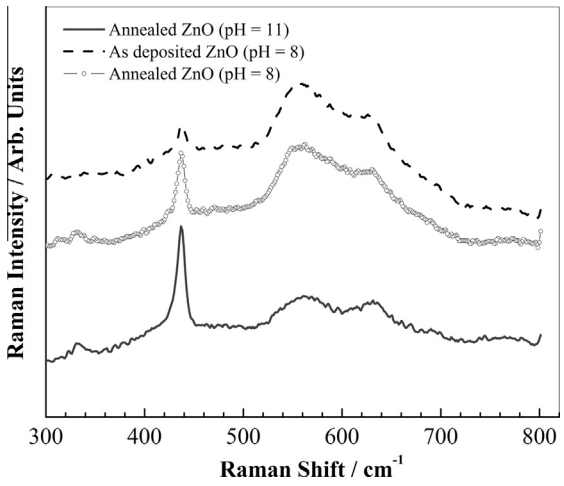

Fig. 4. Raman spectra of ZnO thin films deposited on FTO/glass substrate for as-deposited and annealed samples prepared at pH = 8 and annealed samples prepared at pH = 11.

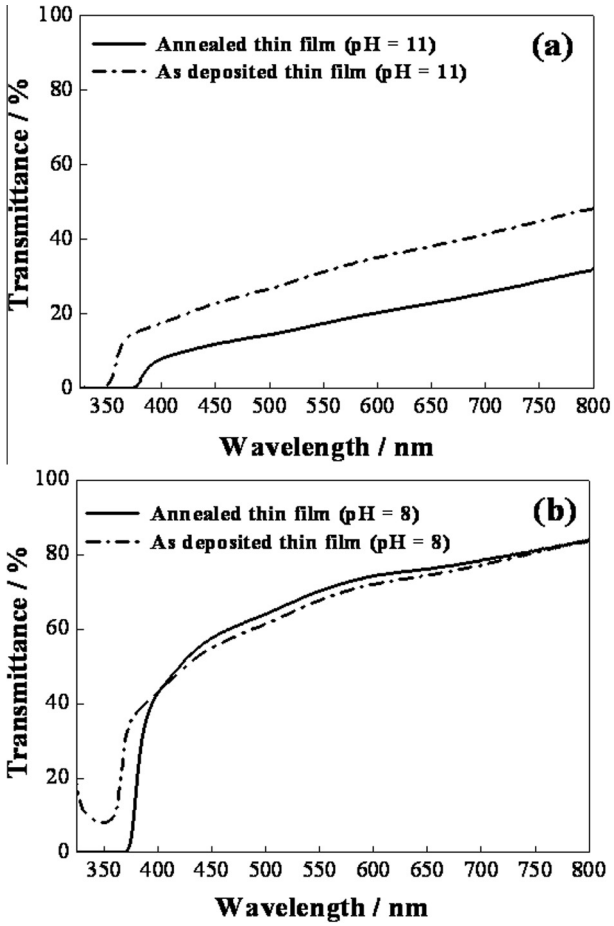

Fig. 5. UV–Vis transmittance spectra of ZnO thin films before (dash-dotted line) and after annealing (full line) prepared at (a) pH = 11 and (b) pH = 8.

3.3.2. Bandgap energy

Fig. 5(a) and (b) indicate that absorption edges shift towards longer wavelength when the films are annealed. This behavior can be analyzed by direct bandgap energy (E_g) determination from absorption based on Tauc's method [26]. In order to achieve a correct determination of the optical bandgap, the zero absorption line should be properly selected. To choose the correct zero line, background absorption α_{back} was introduced in the spectra. This background represents the influence on the absorption of many effects not included in the model for the optical absorption and behaves as an indirect or amorphous semiconductor. Reflections, dispersions and amorphous phases are taken into consideration and extracted from the experimental data [2,27–30]. These effects may arise either in the deposited thin film or even in the substrate. To determine the bandgap of ZnO, a corrected absorption α_{corr} was obtained as $\alpha_{corr} = \alpha_{exp} - \alpha_{back}$ [2,28–30]. The experimental absorption α_{exp} is defined as $-\ln T$ (being T the transmittance spectrum). It is a measurement of the absorption coefficient in arbitrary units (i.e. absorptance instead) as the thickness is not taken in consideration in this definition [31]. The background absorption α_{back} is obtained from a linear fitting of $(\alpha_{exp}h\nu)^{1/2}$ vs. $(h\nu)$ in the transparency region (i.e. below expected ZnO bangap energy) [2,28–30]. The plots of $(\alpha_{corr}h\nu)^2$ vs. $(h\nu)$ are shown in Fig. 6(a) and (b), corresponding to as-deposited and annealed ZnO thin films for pH = 11 and 8, respectively. It can be seen that, irrespective of the pH value, E_g of the as-deposited thin films is higher than those with the annealing treatment. The decrease in E_g after annealing could be due to an increase in the crystallite size and to the presence of less defect sites. This is in good agreement with the experimental results from XRD analysis (see Table 1). Hong et al. [32] observed a shift in the optical bandgap of ZnO thin films from 3.31 to 3.26 eV after annealing and attributed this shift to the increase of the ZnO crystallite size.

E_g increases when the material is formed by crystallites sufficiently small and this behavior can be attributed to some extent quantum confinement [33]. Instead, as crystal size increases, the E_g will approach the bulk E_g. The most accepted and simple

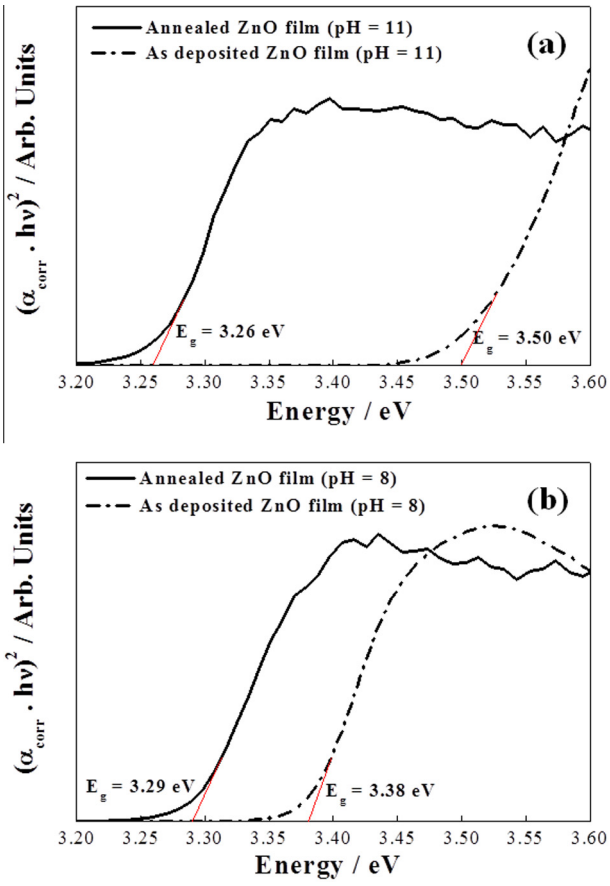

Fig. 6. Plot of $(\alpha_{corr}h\nu)^2$ vs. $(h\nu)$ according to Tauc for as-deposited (dash-dotted line) and annealed (full line) ZnO thin films prepared at (a) pH = 11 and (b) pH = 8.

dependence between absorption edge shift and crystal size is known as Brus dependence [9,34,35]:

$$\Delta E_g = E_g - E_g^{(bulk)} \cong E_b\left(\frac{\pi a_B}{R}\right)^2 - 3.6E_b\left(\frac{a_B}{R}\right) \quad (1)$$

where ΔE_g is the shift in absorption edge, E_g is the measured bandgap energy value, $E_g^{(bulk)}$ is the expected bulk bandgap energy value, E_b is the exciton binding energy, a_B is the exciton Bohr radius and R is the average crystallite radius, which is assumed to have spherical shape. The most accepted values of E_b and a_B for ZnO are 60 meV and 18 Å, respectively [10]. If the lower absorption edge obtained from Fig. 5 is used as $E_g^{(bulk)}$ value in the present case (i. e. $E_g^{(bulk)} \sim 3.26$ eV for annealed sample in Fig. 6a), the measured shifts for as-deposited films prepared at pH = 11 and 8 are 0.24 eV and 0.09 eV, respectively. From Eq. (1), the corresponding crystal diameters $D = 2R$ would be 42 and 54 Å, respectively. The results in Table 1 show that these values agree well with the sizes observed by both TEM and XRD for as-deposited thin films.

Finally, the Urbach parameter E_U was calculated from Fig. 6 using a sigmoidal curve [36,37] for the below bandgap absorption (i.e. where experimental curve departs from linear fitting). The values obtained for E_U are between 25 and 40 meV. These values are relatively low [38], corresponding with a good crystallinity of the samples, and are a measure of the intrinsic uncertainty in bandgap energy.

3.3.3. Photoluminescence

The influence of pH during preparation on the photoluminescence (PL) spectra was also investigated. Fig. 7(a) and (b) show the room-temperature visible PL (VL) spectra (excited at 295 nm) of the as-prepared ZnO thin films for both pH values. The VL is the focus of the discussion that follows because, as it was explained in section 2.4, a filter is placed between the sample and the spectrometer in the PL measurement setup. This filter removes the UV contribution from the LED. But in doing so, it also filters the UV and near UV PL from the sample. Both samples exhibit intense and wide visible emissions (over more than 200 nm). There is a clear dependence of VL spectral shape from the sol pH. When pH = 8 the PL is peaked at 600 nm (2.06 eV, orange–red), while at pH = 11 there is a blue shift, with a maximum value close to 560 nm (2.21 eV, yellow–green) and another clear peak close to 475 nm (2.61 eV, blue) can be observed. Moreover, in the case of pH = 8, the VL has a higher intensity in almost all the visible spectra, except for the blue peak (not shown). In contrast, the annealed samples show no detectable emission.

To interpret these results, the origin of ZnO VL must be reviewed. Far from being widely accepted, this is still a matter of controversy. It is well established that, except for impurities added intentionally, VL is associated to intrinsic defect states [34,39,40]. Oxygen vacancies (V_O), zinc vacancies (V_{Zn}), interstitial zinc (Zn_i) and interstitial oxygen (O_i) are the most common intrinsic defects [39,40]. Generally it is assumed that the electronic states they originate from are shallow donor for Zn_i, shallow acceptor for V_{Zn}, while V_O and O_i originate deep states. In this interpretation, wide visible emissions are caused by: transitions to V_{Zn} for blue emission, to V_O for green–yellow emission, and to O_i for orange–red emission (in every case from electrons excited at the conduction band or the Zn_i state) [39,40]. Some authors attribute the green–yellow emission to V_O, but as an excited deep state in a transition to the valence band [12,41], while others assign this green–yellow emission to deep states due to the antisite oxygen O_{Zn} [42,43]. More recently surface OH^- have also been suggested to be responsible for visible emissions [14,43]. For nanostructured ZnO samples, all these states are present at the surface of the nanostructure and contribute to VL [44], and their relative importance depends on the morphology [12,13]. Deep state shifts are usually smaller than band edge shifts [45]. In all cases, the green, yellow, and red emissions involve one deep state and one band or shallow state. Therefore it is expected that if the absorption edge shifts due to size quantization, the VL should shift in the same direction, but in a lesser amount than absorption edge shift.

The as-deposited samples showed size quantization (see Figs. 5 and 6), with the bandgap energy higher with pH = 11 (3.50 eV) than with pH = 8 (3.38 eV). A similar shift in the VL peak appears in Fig. 7, as expected for size quantization dependence. However, this shift from 600 nm (~2.07 eV) to 560 nm (2.21 eV) is higher than the 0.12 eV observed from Fig. 6. The large changes observed in Fig. 7 may also have a contribution from different defect relative densities in samples prepared using sols with different pH values.

To quantify in depth the differences in the spectra, the signal in Fig. 7 was decomposed into several Gaussian peaks. The best fittings were obtained with three peaks, which fairly correspond to the ones seen when pH = 11, and to those reported in the literature [39,40]. As mentioned above, VL may involve several transitions and many types of defects, which contribute to the controversial nature of the PL mechanism [12]. However, no

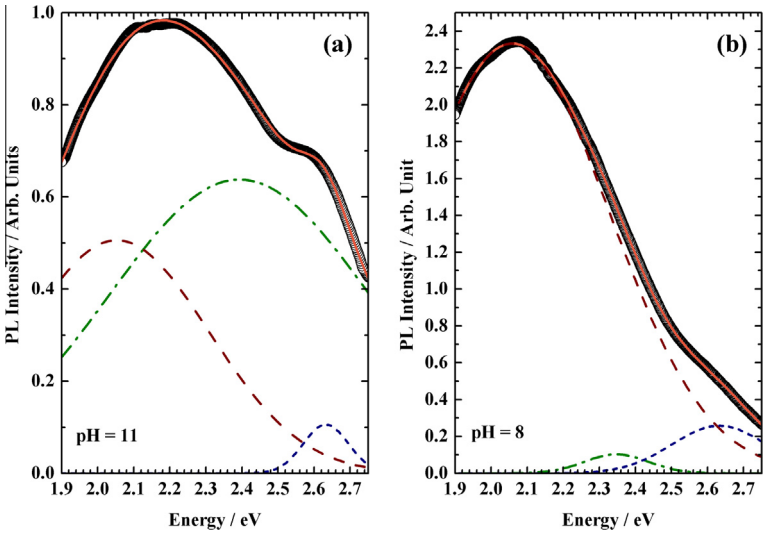

Fig. 7. Normalized VL intensity and Gaussian fit for as-deposited ZnO using 295 nm excitation. (a) pH = 11 with peak positions at 2.05 eV, 2.39 eV and 2.63 eV. (b) pH = 8 with peak positions at 2.06 eV, 2.39 and 2.63 eV.

significant improvement resulted from fitting using more peaks. In this case the three contributions come from the orange–red at ~2.05 eV (~600 nm), green at ~2.35 eV (~520 nm), and blue at 2.63 eV (~470 nm). As discussed above, they may correspond to transitions to O_i, V_O, and V_{Zn} states, respectively, most likely from Zn_i states [39,40]. As the first peak is dominant at pH = 8, a larger density of both O_i and Zn_i may be present in these samples. The intermediate peak suggests that samples prepared at pH = 11 may have also an important content of V_O. This higher density of V_O could eventually be attributed to OH^- [14,43], instead. This, in turn, could be associated to the higher pH associated to the use of NaOH. Furthermore, no clear dependence in peak positions with excitation wavelength was observed, suggesting that size distribution is quite homogeneous.

Finally, the absence of light emission in the case of annealed samples implies the elimination of all these defect states [35]. According to the literature, they may be mainly present in the surface [44], given that a large fraction of the atoms are on the surface when dealing with nanocrystalline materials.

4. Conclusions

Nanocrystalline ZnO thin films have been deposited on conductive fluorine doped tin oxide over glass by means of a simple sol–gel based spin coating technique. The alkalinity of the precursor solutions and the thermal treatment are found to be key factors in the performance of the films. The nature of the precursor solution determines the pH and influences the structural, morphological and optical properties of the films. Annealed films are shown to present smaller size agglomerates than as-deposited films. In contrast, crystallites grow after the annealing treatment. A restructuration process produces more stable states with bigger crystallites grouped into smaller agglomerates.

Raman spectra are in good agreement with others reported in the literature and show the bands typical for wurtzite, independently of pH. The definition of the bands and the relative intensity improve with annealing.

Transmittance spectra present large absorption edges for as-deposited samples which correlate well with nanocrystal sizes evaluated by TEM and XRD. The photoluminescence measurement of as-deposited samples reveals the presence of broad visible emission. According to usual reports of luminescent centers in ZnO all Zn_i, V_{Zn}, and O_i intrinsic defects must be present. However, shape changes in these spectra cannot only be explained by size quantization shifts. A large density of green or yellow centers must be present in the films after preparation at pH = 11, with V_O being the most probable defect originating from these changes. No photoluminescence in the visible part of the spectrum was detected in the case of annealed samples, suggesting that these defects are no longer present after the thermal treatment.

Acknowledgements

In Uruguay this work has been partially supported by CSIC (Comisión Sectorial de Investigación Científica) of the Universidad de la República, in Montevideo, PEDECIBA – Física, and ANII (Agencia Nacional de Investigación e Innovación).

This investigation has also been supported by CONICET (Consejo Nacional de Investigaciones Científicas y Técnicas, Agencia Nacional de Promoción Científica y Tecnológica), ANCyPT (Agencia Nacional de Promoción Científica y Tecnológica) and Universidad Nacional de Mar del Plata from Argentina.

Also, support from MINCyT (Ministerio de Ciencia, Tecnología e Innovación Productiva) in Argentina and DST (Department of Science and Technology) in South Africa are greatly acknowledged.

References

[1] D.P. Norton, Y.W. Heo, M.P. Ivill, K. Ip, S.J. Pearton, M.F. Chislom, T. Steiner, Mater. Today 7 (2004) 34–40.
[2] C.D. Bojorge, V.R. Kent, E. Teliz, H.R. Cánepa, R. Henríquez, H. GÃµmez, R.E. Marotti, E.A. Dalchiele, Phys. Status Solidi A 208 (2011) 1662–1669.
[3] S. Öztürk, N. Kılınç, N. Taşaltin, Z.Z. Öztürk, Thin Solid Films 520 (2011) 932–938.
[4] A. Sharma, B.P. Singh, S. Dhar, A. Gondorf, M. Spasova, Surf. Sci. 606 (2012) L13–L17.
[5] O. Tari, A. Aronne, M.L. Addonizio, S. Daliento, E. Fanelli, P. Pernice, Sol. Energy Mater. Sol. Cells 105 (2012) 179–186.
[6] D.Y. Torres Martínez, R. Castanedo Pérez, G. Torres Delgado, O. Zelaya Ángel, J. Photochem. Photobiol. A 235 (2012) 49–55.
[7] J.B. Baxter, E.S. Aydil, J. Cryst. Growth 274 (2005) 407–411.
[8] Z.L. Wang, Mater. Today 7 (2004) 26–33.
[9] Y.S. Wang, J. Cryst. Growth 291 (2006) 398–404.
[10] Ü. Özgür, Y.I. Alivov, C. Liu, A. Teke, M.A. Reshchikov, S. Doğan, V. Avrutin, S.J. Cho, H. Morko, J. Appl. Phys. 98 (2005) 41301.
[11] J. Lim, K. Shin, H. Woo Kim, C. Lee, J. Lumin. 109 (2004) 181–185.
[12] N.S. Han, H.S. Shim, J.H. Seo, S.Y. Kim, S.M. Park, J.K. Song, J. Appl. Phys. 107 (2010) 084306.
[13] A.B. Djurišić, Y.H. Leung, K.H. Tam, L. Ding, W.K. Ge, H.Y. Chen, S. Gwo, Appl. Phys. Lett. 88 (2006) 103107.
[14] A.B. Djurišić, Y.H. Leung, K.H. Tam, Y.F. Hsu, L. Ding, W.K. Ge, Y.C. Zhong, K.S. Wong, W.K. Chan, H.L. Tam, K.W. Cheah, W.M. Kwok, D.L. Phillips, Nanotechnology 18 (2007) 095702.
[15] L. Xu, G. Zheng, J. Miao, F. Xian, Appl. Surf. Sci. 258 (2012) 7760–7765.
[16] P.T. Hsieh, Y.C. Chen, M.S. Lee, K.S. Kao, M.C. Kao, M.P. Houng, J. Sol–Gel Sci. Technol. 47 (2008) 1–6.
[17] T. Ivanova, A. Harizanova, T. Koutzarova, B. Vertruyen, Mater. Lett. 64 (2010) 1147–1149.
[18] M. Sharma, R.M. Mehra, Appl. Surf. Sci. 255 (2008) 2527–2532.
[19] G. Li, X. Zhu, X. Tang, W. Song, Z. Yang, J. Dai, Y. Sun, X. Pan, S. Dai, J. Alloys Compd. 509 (2011) 4816–4823.
[20] S. Ilican, F. Yakuphanoglu, M. Caglar, Y. Caglar, J. Alloys Compd. 509 (2011) 5290–5294.
[21] S. Rani, P. Suri, P.K. Shishodia, R.M. Mehra, Sol. Energy Mater. Sol. Cells 92 (2008) 1639–1645.
[22] G.H. Mhlongo, O.M. Ntwaeaborwa, H.C. Swart, R.E. Kroon, P. Solarz, W. Ryba-Romanowski, K.T. Hillie, J. Phys. Chem. C 115 (2011) 17625–17632.
[23] A.L. Patterson, Phys. Rev. 56 (1939) 978–982.
[24] O. Lupan, T. Pauporté, B. Viana, P. Aschehoug, Electrochim. Acta 56 (2011) 10543–10549.
[25] L.C. Nehru, M. Umadevi, C. Sanjeeviraja, Inter. J. Mater. Eng. 2 (2012) 12–17.
[26] J. Tauc, R. Grigorovici, A. Vancu, Phys. Status Solidi B 15 (1966) 627–637.
[27] X. Zhang, S. Hou, H. Mao, J. Wang, Z. Zhu, Appl. Surf. Sci. 256 (2010) 3862–3865.
[28] G. Guerguerian, F. Elhordoy, C.J. Pereyra, R.E. Marotti, F. Martín, D. Leinen, J.R. Ramos-Barrado, E.A. Dalchiele, J. Phys. D: Appl. Phys. 45 (2012) 245301.
[29] G. Guerguerian, F. Elhordoy, C.J. Pereyra, R.E. Marotti, F. Martín, D. Leinen, J.R. Ramos-Barrado, E.A. Dalchiele, Nanotechnology 22 (2011) 505401.
[30] C.D. Bojorge, H.R. Cánepa, U.E. Gilabert, D. Silva, E.A. Dalchiele, R.E. Marotti, J. Mater. Sci. Mater. Electron. 18 (2007) 1119–1125.
[31] J. Pankove, Optical Processes in Semiconductors, Dover edition, New Yersey, 1971.
[32] R. Hong, J. Huang, H. He, Z. Fan, J. Shao, Appl. Surf. Sci. 242 (2005) 346–352.
[33] E.M. Wong, P.C. Searson, Appl. Phys. Lett. 74 (1999) 2939–2941.
[34] L. Brus, J. Phys. Chem. 90 (1986) 2555–2560.
[35] Y.S. Wang, P.J. Thomas, P. O'Brien, J. Phys. Chem. B 110 (2006) 4099–4104.
[36] R.W. Martin, P.G. Middleton, K.P. O'Donnell, W. Van Der Stricht, Appl. Phys. Lett. 74 (1999) 263–265.
[37] H.P. He, F. Zhuge, Z.Z. Ye, L.P. Zhu, F.Z. Wang, B.H. Zhao, J.Y. Huang, J. Appl. Phys. 99 (2006) 023503.
[38] E. Rabinovich, G. Hodes, J. Phys. Chem. C 117 (2013) 1611–1620.
[39] C.H. Ahn, Y.Y. Kim, D.C. Kim, S.K. Mohanta, H.K. Cho, J. Appl. Phys. 105 (2009) 013502.
[40] N.H. Alvi, K. ul Hasan, O. Nur, M. Willander, Nanoscale Res. Lett. 6 (2011) X1–X7.
[41] H.S. Kang, J.S. Kang, J.W. Kim, S.Y. Lee, J. Appl. Phys. 95 (2004) 1246–1250.
[42] B. Lin, Z. Fu, Y. Jia, Appl. Phys. Lett. 79 (2001) 943–945.
[43] C.V. Manzano, D. Alegre, O. Caballero-Calero, B. Alén, M.S. Martín-González, J. Appl. Phys. 110 (2011) 043538.
[44] Y. Gong, T. Andelman, G.F. Neumark, S. O'Brien, I.L. Kuskovsky, Nanoscale Res. Lett. 2 (2007) 297–302.
[45] P.Y. Yu, M. Cardona, Fundamentals of Semiconductors: Physics and Materials Properties, third ed., Springer, New York, 2005.